NANO LETTERS

Letter

pubs.acs.org/NanoLett

Observation and Quantification of Nanoscale Processes in Lithium Batteries by Operando Electrochemical (S)TEM

B. L. Mehdi,*[,†] J. Qian,[‡] E. Nasybulin,[‡] C. Park,[§] D. A. Welch,[∥] R. Faller,[∥] H. Mehta,[⊥] W. A. Henderson,[‡] W. Xu,[‡] C. M. Wang,[⊥] J. E. Evans,[⊥] J. Liu,[‡] J. -G. Zhang,[‡] K. T. Mueller,[⊥,#] and N. D. Browning[†]

[†]Joint Center for Energy Storage Research, Fundamental and Computational Science Directorate, Pacific Northwest National Laboratory, Richland, Washington 99352, United States

[‡]Joint Center for Energy Storage Research, Energy and Environmental Directorate, Pacific Northwest National Laboratory, Richland, Washington 99352, United States

[§]Department of Industrial and Manufacturing Engineering, Florida State University, Tallahassee, Florida 32306, United States

[∥]Department of Chemical Engineering and Materials Science, University of California, Davis, California 95616, United States

[⊥]Joint Center for Energy Storage Research, Environmental Molecular Sciences Laboratory, Pacific Northwest National Laboratory, Richland, Washington 99352, United States

[#]Department of Chemistry, Penn State University, University Park, Pennsylvania 16802, United States

Supporting Information

ABSTRACT: An operando electrochemical stage for the transmission electron microscope has been configured to form a "Li battery" that is used to quantify the electrochemical processes that occur at the anode during charge/discharge cycling. Of particular importance for these observations is the identification of an image contrast reversal that originates from solid Li being less dense than the surrounding liquid electrolyte and electrode surface. This contrast allows Li to be identified from Li-containing compounds that make up the solid-electrolyte interphase (SEI) layer. By correlating images showing the sequence of Li electrodeposition and the evolution of the SEI layer with simultaneously acquired and calibrated cyclic voltammograms, electrodeposition, and electrolyte breakdown processes can be quantified directly on the nanoscale. This approach opens up intriguing new possibilities to rapidly visualize and test the electrochemical performance of a wide range of electrode/electrolyte combinations for next generation battery systems.

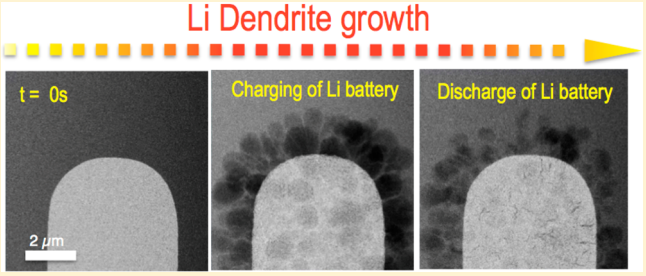

KEYWORDS: *Operando scanning transmission electron microscopy, SEI layer, in situ electrochemical liquid cell, Li batteries, Li dendrite formation, Li deposition/dissolution*

Lithium (Li)-ion batteries are currently used for a wide variety of portable electronic devices, electric vehicles and renewable energy applications.[1,2] Extensive worldwide research efforts are now being devoted to more advanced "beyond Li-ion" battery chemistries, such as lithium−sulfur (Li−S)[3] and lithium−air (Li−O_2),[4] in which the carbon anode in which Li^+ cations intercalate is replaced with Li metal. So far the practical use of this electrode has been highly problematic. The main challenges at the anode/electrolyte interface involve controlling the formation of a solid-electrolyte interphase (SEI) layer (formed by the reaction of Li metal with electrolyte components) and the evolution of Li metal dendrites. The SEI layer formation continuously consumes both the Li metal and electrolyte, while resulting in a highly resistive layer that leads to the rapid degradation in Li electrode cycling performance.[5] The growth of Li metal dendrites can also contribute to an increase in the rate of capacity fading (i.e., due to the formation of "dead Li" that loses electrical contact with the electrode) and can cause internal short circuits (when the dendrites contact the cathode) if they continue to grow, leading to extreme safety issues.[6] Obtaining a detailed understanding of the fundamental processes occurring at the electrode/electrolyte interfaces, especially for the evolution of the SEI and initial stages of Li dendrite formation, is therefore a key step in mitigating the degradation in performance (increasing the lifetime) and addressing safety concerns for Li batteries.

Both transmission electron microscopy (TEM)[7] and scanning transmission electron microscopy (STEM)[8] have been used for many years to solve atomic scale interface problems in materials science. For the case of Li batteries, imaging the anode−electrolyte interface is complicated by the fact that the problem involves a solid−liquid interface rather than a solid−solid interface (the presence of the liquid creates

Received: January 15, 2015
Revised: February 17, 2015

DOI: 10.1021/acs.nanolett.5b00175
Nano Lett. XXXX, XXX, XXX−XXX

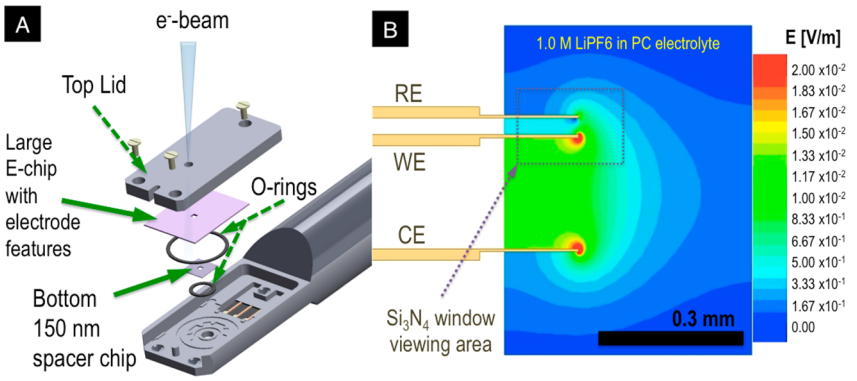

Figure 1. (a) Schematic illustration of the in situ ec-liquid (S)TEM stage. (b) ANSYS Maxwell static 3D electromagnetic finite element simulation of the electric field distribution in the in situ ec-liquid (S)TEM cell containg the $LiPF_6$/PC electrolyte during the galvanostatic discharge at >0.1 mA/cm^2 with the hot spot localized at the top of the Pt working electrode. The legend shows that during electrochemical cycling the in situ ec-liquid cell exhibits a nonuniform electric field distribution along the Pt working electrode. However, as Li deposition (shown in Figure 2) is observed along the entire length of the Pt electrode, this indicates that a wide range of current densities can be used to initiate the deposition.

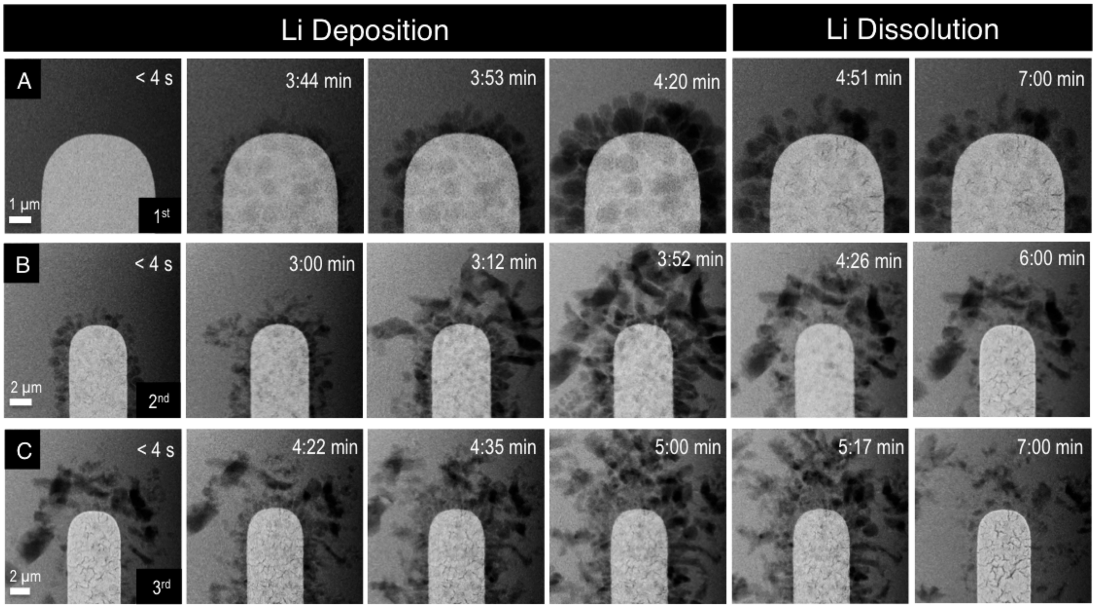

Figure 2. High-angle annular dark field (HAADF) images of Li deposition and dissolution at the interface between the Pt working electrode and the $LiPF_6$/PC electrolyte during the (a) first, (b) second, and (c) third charge/discharge cycles of the operando cell. The formation of the SEI layer (ring of contrast around the electrode), alloy formation due to Li^+ ion insertion, and the presence of "dead Li" detached from the electrode can all be seen in the images at the end of the cycle, thereby demonstrating the degree of irreversibility associated with this process.

imaging difficulties even for the most advanced aberration corrected instruments[7,8]). However, recent years have seen a growth in the use of in situ liquid stages[9] that have allowed nucleation and growth phenomena,[10−13] biological systems[14] and electrochemical (ec) reactions to be observed.[15−21] By carefully calibrating the effect of the electron beam being used to make the observations, it is now possible to make truly quantitative operando observations using these liquid stages.[19] In this paper, we use in situ ec-(S)TEM to study the initial stages of SEI formation and Li dendrite evolution at the anode/electrolyte interface during the electrodeposition process. To make sure that the electron beam does not have any effect on these initial results, the electron beam dose rate is carefully calibrated to be below the electrolyte damage threshold prior to operando electrochemical cycling[19] (in this case all experiments use a dose ≤0.3 electrons/Å^2/s). As such, typical beam effects such as the formation of bubbles and/or precipitates from the breakdown of the electrolyte are completely avoided.

To quantify the electrochemistry that occurs in the operando stage, we need to fully understand the distribution of electric fields at the electrodes. The in situ TEM liquid holder (Figure 1a) used for this experiment was supplied by a commercial vendor (more details on the stage design are given in Supporting Information). To provide insight into the location of the deposition reactions that take place during cycling of the electrochemical cell, an Ansoft Maxwell static three-dimensional (3D) electromagnetic finite element simulation was used to extract quantitative information about the electric field distribution along the Pt working electrode in the ec-microchip. The simulation (illustrated in Figure 1b) shows the electric field distribution within the electrolyte during a galvanostatic discharge at a constant current of 0.1 mA/cm^2. This analysis shows that the electrode configuration exhibits a localized enhancement of the electric field gradient and nonuniform electric field distribution along the Pt working electrode surface

DOI: 10.1021/acs.nanolett.5b00175
Nano Lett. XXXX, XXX, XXX−XXX

with a "hot spot" localized at the top (more details of the modeling are given in Supporting Information).

After confirming that a deposition reaction is feasible, we obtained high-angle annular dark field (HAADF) STEM images of the anode/electrolyte interface during the first three charge–discharge cycles of this operando Li battery. The first set of images (Figure 2a) shows uniform deposition of Li along the Pt electrode during what is considered to be the charging process. However, during the first discharge, dissolution of Li (i.e., the formation of Li^+ ions) is not perfectly reversible as remnant Li is observed at the anode/electrolyte interface (the direct link between the position in the cyclic voltammogram (CV) and the deposition/dissolution of Li is shown in Supporting Information, movies si_002, si_003, and si_004). This residual amount of Li increases the surface roughness and the electroactive surface area of the Pt electrode, leading to preferential enhanced Li growth during the deposition in the second cycle (note the magnification change between the first and second cycles). By the time the second cycle is complete, the interface now contains large sections of material attached to the interface (Figure 2b). Interestingly, we can also identify patches of "dead Li" around the electrode in the final images in all three cycles. These are deposits that are no longer attached to the Pt electrode and so are electrochemically inactive (they do not participate in the subsequent charge–discharge cycles). As the third cycle proceeds, shown in Figure 2c, we again observe rapid growth of the Li deposits and significant "dead Li" after the cycle is complete. In addition to these processes, Pt is known to alloy with Li and the insertion of Li^+ ions can be recognized by the expansion of the Pt electrode during the deposition/charging process and shrinking during the dissolution/discharge process.

The STEM images shown in Figure 2 are formed by mass–thickness contrast; typically, a material that is either thicker or has a higher atomic number, Z, (or both) scatters electrons into/out of the detector to form the dark-field/bright-field image. In the bright-field image (so named because the background in the image representing zero scattering is bright), this means that the heaviest/most dense/thickest materials appear dark while in the dark-field image (so named because the background in the image representing zero scattering is dark) the heaviest/most dense/thickest materials appear bright. Here, however, close inspection of the contrast in the dark-field (and bright-field) images shows that the contrast is in fact reversed for the particles deposited during the electrochemical cycle. In the bright-field image, the particles are brighter than the background while in the dark-field image they are darker than the background. To obtain a contrast reversal of this type, the electrodeposited material must be lighter/less dense than the electrolyte surrounding it. In the electrochemical processes for Li batteries in general and in this operando cell in particular, the only solid material that is less dense than the electrolyte is Li metal.

The identification of Li metal from the contrast of the images shown in Figure 2 can be confirmed by the simulations shown in Figure 3[22] (more details on the simulation parameters are given in Supporting Information). Here some dust left over from the microfabrication process for the cell windows (probably either Si, SiO_x, or Si_xN_y) is shown in the dark-field images with the correct contrast (the dust is on the outside of the windows and has no effect on the electrochemistry in the cell). After the electrochemical deposition process, the nanoparticles formed at the working electrode can be seen

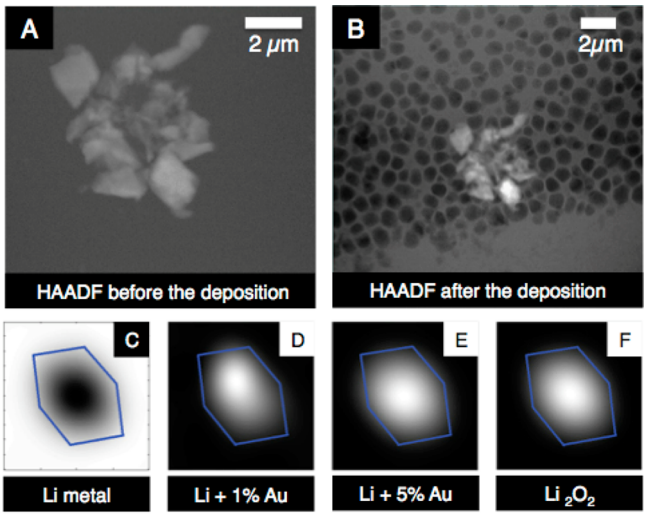

G	Li	Li_2CO_3	Li_2O_2	LiF	Li_2O	LiTf in TEGDME
Density [g/cm³]	0.53	2.11	2.31	2.64	2.01	1.01

Figure 3. Images (a) and (b) show the particle on the outside of the window before and after the deposition of Li metal nanoparticles from a lithium trifluoromethanesulfonate (LiTf) in tetraglyme (TEGDME, saturated with O_2) electrolyte. The contrast of the dust particle in the HAADF image (a) appears brighter than the background (electrolyte, LiTf in TEGDEM/O_2), which is due to the higher density of the particle than the surrounding electrolyte. After the Li deposition, the contrast of the dust particle versus the electrolyte solution remains the same (b). However, the Li metal shows contrast reversal because it has a lower density (0.51 g/cm^3) than both the LiTf in TEGDEM/O_2 electrolyte (1.01 g/cm^3) and the dust particle. Simulations of the contrast expected for dark-field images of 5 nm nanoparticles composed of (c) Li, (d) Li + 1% Au, (e) Li + 5% Au, and (f) Li_2O_2 shows contrast reversal only happens for pure Li metal. This is because only Li metal (of all the possible breakdown products) is less dense than the electrolyte (g).

beneath the dust as having the reversed contrast while the dust itself has the correct mass–thickness contrast. Given that the contrast occurs in the location where the assumption is that the material being deposited is a Li dendrite, we can perform image simulations to evaluate whether this is the case. Also shown in Figure 3 is a dark-field simulation for a 10 nm Li particle embedded in an electrolyte with a density of ~1 g/cm^3. It is evident from the simulations that pure Li causes the contrast reversal that is seen in Figure 2. Additionally, if there is the presence of a Li alloy (Li is known to alloy with Au and Pt electrodes) then the contrast would revert to the normal expectation for mass–thickness contrast with only a 1% content from the heavier metal (Figure 3d–f). If we consider the density of Li metal and the other possible electrolyte breakdown products in this system, only Li metal has a density that is lower than the electrolyte. This means that the amount of Li metal that is deposited on the electrode can be quantified directly from these images (more details on the simulations are given in Supporting Information).

Figure 4 shows another experiment performed in the operando ec-cell under the same conditions but with extended cycling. After extended cycling of the cell, we can see clearly the structural changes occurring at the electrode. In addition to observing the Li around the electrode (with reversed contrast), we can also see the SEI layer (the SEI layer is observed as the

DOI: 10.1021/acs.nanolett.5b00175
Nano Lett. XXXX, XXX, XXX–XXX

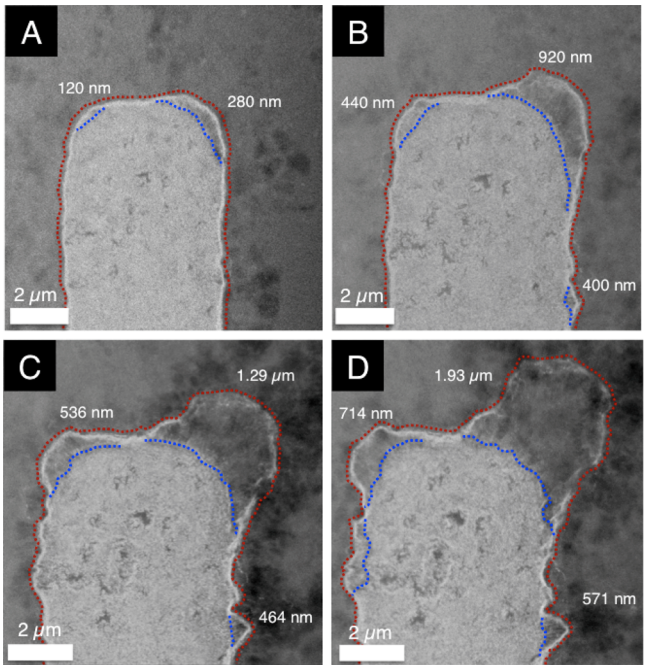

Figure 4. (a) −(d) HAADF images of the interface between the Pt working electrode and the $LiPF_6$/PC electrolyte after cycles 5−8. The growth of a Li subsurface structure (dendrite)[26] can be clearly seen at the position of the electric field hot spot in Figure 1. Additionally, the SEI layer is well formed and clearly seen as is the presence of Li insertion/alloy formation with the Pt electrode and dead Li not in contact with the electrode (the lines are added to emphasize the main structural features; the red line shows the outside of the bright contrast SEI layer while the blue line shows the outline of the Pt electrode).

bright line around the electrode and highlighted with the red dotted line) and a Li protrusion that has been formed beneath the SEI layer at the location of the hot spot shown in Figure 1.[23−25] Cracks in the SEI layer caused by the stresses of Li diffusion[26] are also observed, as are the presence of small nanoparticles separated from the interface that have a similar contrast as the SEI layer and "dead Li" (again clearly identified by the contrast mechanism). In addition, Li insertion into the Pt electrode has now become significant (the interface is expanded and nonuniform as marked by the dotted blue line) and isolated patches of Li are present within the anode.

By using a multitarget tracking algorithm,[27] we located and tracked the trajectories of the growing Li deposits from the video sequences illustrated in Figure 2 (and Supporting Information movies si_002, si_003, and si_004) to determine the overall amount of Li deposited during each cycle (Figure 5). From the quantified Li deposition curves shown in Figure 5b, we find a critical difference between the first cycle and the subsequent second and third cycles. As expected from the images in Figure 2, the initial deposition takes place on a smooth Pt electrode and results in an even distribution of Li on the surface. The subsequent cycling of the Pt electrode results in uneven deposition of Li due to increased surface roughness (which is a consequence of the irreversible process of Li deposition in the previous cycle) with an increased amount of dead Li around the electrode surface. Similar conclusions on the irreversibility of the charge−discharge cycles and the amount of Li deposited can be extracted from the three CV cycles shown in Figure 5a. In particular, the difference between the sum of the currents passed through the ec-cell during the Li

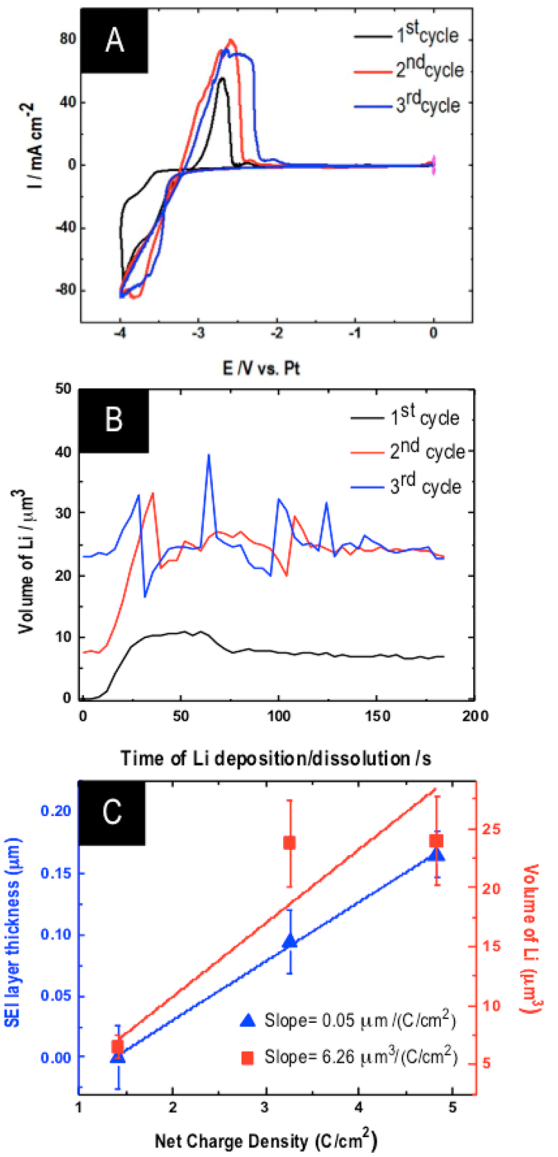

Figure 5. (a) CVs for the first three cycles shown in Figure 2. (b) The area of Li deposited at the Pt electrode−$LiPF_6$/PC electrolyte interface measured by the tracking algorithm (note that the variability in the third scan and the small increase in overall Li deposit is likely caused by some of the Li being pushed out of the field of view). (c) The net charge density measured from the CV curves ($= |\Sigma_V i_V|/\upsilon \times A_{electrode}$), where the υ is the scan rate of 20 mV/s and $A_{electrode}$ is the area of the electrode, is plotted against the amount of Li electrodeposited (here for simplicity we assume that the Li deposits are the nominal thickness of the cell = 650 ± 100 nm and multiply this by the area determined from the algorithm in part (b)) and the thickness of the SEI layer (here the error bars are estimated from the standard deviation and are ±25 nm at most). The plots show a change in the relative importance of these secondary mechanisms (i.e., mechanisms that decrease the Coulombic efficiency) with the total current deposited in the cell (note the total electrode area is 250 μm^2 and the total time for the scan was 400 s).

deposition and dissolution processes gives a direct indication of the level of irreversibility of each charge/discharge cycle. Furthermore, Li−Pt dealloying[28] from the Pt electrode can be recognized by the two characteristic peaks between −2.0 and −2.5 V (more visible in the second and third CV cycles). Interestingly, when we measure the expansion (alloying) and

DOI: 10.1021/acs.nanolett.5b00175
Nano Lett. XXXX, XXX, XXX−XXX

contraction (dealloying) of the electrode from the movies (si_002, si_003, and si_004) we note that the size of the Pt electrode is essentially the same after the cycle has completed, indicating that the process is reversible within the limits of these TEM measurements. Hence, although Pt electrodes are not standard for Li batteries, they do not appear to have a significant effect upon the irreversible processes taking place here during the first three cycles (as is shown in Figure 4, extended cycling does show a noticeable and irreversible effect).

From the difference between the total current that was required to initiate the Li deposition and dissolution shown in Figure 5a, we can quantify the net current that takes part in all of the irreversible processes that are occurring. Figure 5c shows the plot of the net charge density against the amount of Li that we measure from the tracking algorithms to be deposited in the cell after each cycle (the electrode area is 250 μm^2 and the total time for the scan was 400 s). As we can see clearly in Figure 4, the images also allow for the identification of the SEI layer (the SEI layer is also observed in Figure 2, but at the magnification of the images shown in Figure 2 it cannot be seen. A higher-magnification image that shows the identification of the SEI layer is shown in the Supporting Information Figure S1). This layer does not exhibit the same "reversed" contrast as the Li deposits and hence must be composed of a material that is denser than the electrolyte, making it straightforward to identify the Li deposits from the SEI layer. Using the same tracking algorithm we can precisely measure the thickness of this layer as a function of the total current passed through the cell (plotted in Figure 5c). As a first approximation, we can assume the behavior is linear and quantify directly the growth of the SEI layer to be 0.05 $\mu m/(C/cm^2)$ and the amount of Li deposited to be 6.26 $\mu m^3/(C/cm^2)$ from the slope of the fit to the experimental results (here the r^2 value for the SEI layer line fit is 0.99 while for the amount of Li deposited the r^2 value is 0.82. The smaller r^2 value for the Li deposit is likely caused by Li being pushed out of the window of observation during the third cycle). Both of these measures can be used as figures of merit for the stability of the electrode−electrolyte interface. Interestingly, we can see from Figure 4 that the SEI layer thickness stabilizes (presumably around the fourth cycle for this experiment) and does not significantly grow with further cycling. With the extended cycling, however, we can see the diffusion of Li through the SEI layer and the formation of a granular Li protrusion (Figure 4).

In conclusion, we have shown that by creating the battery within an in situ stage for the scanning transmission electron microscope (STEM), we have been able to quantify the features that control the performance of Li-containing energy storage systems. Most notably, we have identified the contrast mechanism that allows the mass of Li involved in electrodeposition and the evolution of the SEI layer to be quantified directly from the images and correlated with the electrochemical parameters of the cell. Future improvements in cell fabrication (electrodes with different alloying performance and control of the thickness) coupled with the use of faster imaging methods,[29] should permit the initial stages of each of the mechanisms to be quantified on the nanometer to atomic scale. Such analyses, coupled with the use of varying electrolyte compositions (i.e., solvents, salts and additives), may provide critical insights into the complex interfacial reactions needed for future Li-based and next generation energy storage systems.

■ ASSOCIATED CONTENT

Ⓢ Supporting Information

Supporting movies show the correlation between the CV scans and the electrodeposition of Li. Additional details on the in situ electrochemical cell, modeling of the field distribution in the cell, and simulating the contrast in the STEM images are provided. This material is available free of charge via the Internet at http://pubs.acs.org.

■ AUTHOR INFORMATION

Corresponding Author

*E-mail: layla.mehdi@pnnl.gov.

Author Contributions

B.L.M. and N.D.B. designed the experiments (performed by B.L.M.) and wrote the manuscript. E.N. and J.Q. prepared the electrolyte. C.P. wrote the tracking algorithm and performed the analysis. D.A.W. and R.F. performed the image simulations. H.M. performed the finite element analysis. W.A.H. and J.G.Z. assisted with the interpretation of the CV measurements. All authors discussed the results and commented on the manuscript.

Notes

The authors declare no competing financial interest.

■ ACKNOWLEDGMENTS

This work was primarily supported by Joint Center for Energy Storage Research (JCESR), an Energy Innovation Hub funded by the Department of Energy, Office of Science, Basic Energy Sciences. The development of the operando stage was supported by the Chemical Imaging Initiative, a Laboratory Directed Research and Development Program at Pacific Northwest National Laboratory (PNNL). PNNL is a multiprogram national laboratory operated by Battelle for the U.S. Department of Energy (DOE) under Contract DE-AC05-76RL01830. A portion of the research was performed using the Environmental Molecular Sciences Laboratory (EMSL), a national scientific user facility sponsored by the Department of Energy's Office of Biological and Environmental Research and located at PNNL. The development of the multitarget tracking algorithm is supported by the National Science Foundation under NSF-1334012.

■ REFERENCES

(1) Tarascon, J. M.; Armand, M. *Nature* **2001**, *414*, 359−367.
(2) Goodenough, J. B.; Kim, Y. *Chem. Mater.* **2010**, *22*, 587−603.
(3) Jie, X. L.; Nazar, L. F. *J. Mater. Chem.* **2010**, *20*, 9821−9826.
(4) Bruce, P. G.; Freunberger, S. A.; Hardwick, L. J.; Tarascon, J. M. *Nat. Mater.* **2012**, *11*, 19−29.
(5) Verma, P.; Maire, P.; Novak, P. *Electrochim. Acta* **2010**, *55*, 6332−6341.
(6) Wen, J.; Yu, Y.; Chen, C. *Mater. Express* **2012**, *2*, 197−212.
(7) Haider, M.; Uhlemann, S.; Schwan, E.; Rose, H.; Kabius, B.; Urban, K. *Nature* **1998**, *392*, 768−769.
(8) Batson, P. E.; Dellby, N.; Krivanek, O. L. *Nature* **2002**, *418*, 617−620.
(9) de Jonge, N.; Ross, F. M. *Nat. Nanotechnol.* **2011**, *6*, 695−704.
(10) Evans, J. E.; Jungjohann, K. L.; Browning, N. D.; Arslan, I. *Nano Lett.* **2011**, *11*, 2809−2813.
(11) Zheng, H. M.; Smith, R. K.; Jun, Y. W.; Kisielowski, C.; Dahmen, U.; Alivisatos, A. P. *Science* **2009**, *324*, 1309−1312.
(12) Li, D. S.; Nielsen, M. H.; Lee, J. R. I.; Frandsen, C.; Banfield, J. F.; De Yoreo, J. J. *Science* **2012**, *336*, 1014−1018.
(13) Woehl, T. J.; Park, C.; Evans, J. E.; Arslan, I.; Ristenpart, W. D.; Browning, N. D. *Nano Lett.* **2014**, *14*, 373−378 (2014).

DOI: 10.1021/acs.nanolett.5b00175
Nano Lett. XXXX, XXX, XXX−XXX

(14) de Jonge, N.; Peckys, D. B.; Kremers, G. J.; Piston, D. W. *Proc. Natl. Acad. Sci. U.S.A.* **2009**, *106*, 2159−2164.
(15) Williamson, M. J.; Tromp, R. M.; Vereecken, P. M.; Hull, R.; Ross, F. M. *Nat. Mater.* **2003**, *2*, 532−536.
(16) Huang, J. Y.; Zhong, L.; Wang, C. M.; Sullivan, J. P.; Xu, W.; Zhang, L. Q.; Mao, S. X.; Hudak, N. S.; Liu, X. H.; Subramanian, A.; Fan, H.; Qi, L.; Kushima, A.; Li, J. *Science* **2010**, *330*, 1515−1520.
(17) White, E. R.; Singer, S. B.; Augustyn, V.; Hubbard, W. A.; Mecklenburg, M.; Dunn, B.; Regan, B. C. *ACS Nano* **2012**, *6*, 6308−6317.
(18) Gu, M.; Parent, L. R.; Mehdi, B. L.; Unocic, R.; McDowell, M.; Sacci, R.; Xu, W.; Connell, J.; Xu, P.; Abellan, P.; Chen, X.; Yaohui, Z.; Perea, D.; Lauhon, L.; Zhang, J.; Liu, J.; Browning, N. D.; Cui, Y.; Arslan, I.; Wang, C. *Nano Lett.* **2013**, *13*, 6106−6112.
(19) Abellán, P.; Park, C.; Mehdi, B. L.; Xu, W.; Zhang, Y.; Parent, L. R.; Gu, M.; Arslan, I.; Zhang, J.; Wang, C. M.; Evans, J. E.; Browning, N. D. *Nano Lett.* **2014**, *14*, 1293−1299.
(20) Sutter, E.; Jungjohann, K. L.; Bliznakov, S.; Courty, A.; Maisonhaite, E.; Tenney, S.; Sutter, P. *Nat. Commun.* **2014**, *5*, 4946−4950.
(21) Zeng, Z.; Liang, W.-I.; Liao, H. G.; Xin, H. L.; Chu, Y.-H.; Zheng, H. *Nano Lett.* **2014**, *14*, 1475−1480.
(22) Welch, D. A.; Faller, R.; Evans, J. E.; Browning, N. D. *Ultramicroscopy* **2013**, *135*, 36−42.
(23) Harry, K. J.; Hallinan, D. T.; Parkinson, D. Y.; McDowell, A. A.; Balsara, N. P. *Nat. Mater.* **2014**, *13*, 69−73.
(24) Zheng, G. S.; Lee, W.; Liang, Z.; Lee, H.-W.; Yan, K.; Yao, H.; Wang, H.; Li, W.; Chu, S.; Cui, Y. *Nat. Nanotechnol.* **2014**, *9*, 618−623.
(25) Ansari, Y.; Guo, B.; Cho, J. H.; Park, K.; Song, J.; Ellison, C. J.; Goodenough, J. B. *J. Electrochem. Soc.* **2014**, *161*, A1655−A1661.
(26) Wu, H.; Zhuo, D.; Kong, D.; Cui, Y. *Nat. Commun.* **2014**, *5*, 5193−5196.
(27) Park, C.; Woehl, T. J.; Evans, J. E.; Browning, N. D. *IEEE Trans. Pattern Anal. Mach. Intell.* **2015**, *37*, 611−624.
(28) Kuwata, N.; Iwagami, N.; Matsuda, Y.; Tanji, Y.; Kawamura, K. *ECS Trans.* **2009**, *16*, 53−60.
(29) Kim, J. S.; LaGrange, T. B.; Reed, B. W.; Browning, N. D.; Taheri, M. L.; Armstrong, M. R.; King, W. E.; Campbell, G. H. *Science* **2008**, *321*, 1472−1475.

DOI: 10.1021/acs.nanolett.5b00175
Nano Lett. XXXX, XXX, XXX−XXX